Published by Electrochemical Society. Final version available at: http://dx.doi.org/10.1149/1.3291977

Impact of liquid water on reactant mass transfer in PEM fuel cell electrodes

Jeff T. Gostick[2,3], Marios A. Ioannidis, Mark D. Pritzker[1,2] and Michael W. Fowler

Department of Chemical Engineering, University of Waterloo, Waterloo, ON, Canada N2L 3G1

[1]Corresponding Author: pritzker@uwaterloo.ca

[2]Electrochemical Society Member

[3]Current Address: Lawrence Berkeley National Lab, Berkeley, CA, USA

Keywords: gas diffusion layer, porous media, pore network modeling, percolation, condensation, drainage

Abstract

The breakthrough conditions (capillary pressure and liquid water saturation) in fibrous gas diffusion media (GDM) used in polymer electrolyte membrane fuel cell (PEMFC) electrodes have been studied experimentally by two independent techniques and numerically by pore network modeling. Experiments show that treatment of the GDMs with a hydrophobic polymer coating reduces the water saturation at breakthrough by 50%. Invasion percolation modeling is employed to simulate the breakthrough process and determine mass transfer rates through the partially saturated network. This model shows that the water saturation at breakthrough is drastically reduced when a microporous layer (MPL) is incorporated in the GDM, in agreement with experiments. However, the simulations yield limiting currents significantly higher than those observed in practice whether or not an MPL is present. Further calculations to include the contribution of condensation to water saturation within the GDM also result in unrealistically high limiting currents and suggest that mass transfer resistance in the catalyst layer that is not included in the model plays an important role. If condensation is the principal mode for water accumulation within the GDM, simulations show that the MPL has only a small impact on liquid water distribution and does not improve performance, contrary to expectation.

1. Introduction

The behavior of water in the porous electrodes of polymer electrolyte membrane fuel cells (PEMFCs) has been the subject of intense research efforts. The electrochemical production of water on the cathode side, combined with high humidity levels of the inlet gas streams, can lead to liquid water formation and accumulation inside the cell. The presence of liquid water in the porous catalyst layer (CL) and gas diffusion media (GDM) causes the effective diffusion coefficient of oxygen and therefore the maximum attainable current to decrease sharply.[1] Decreasing the amount of platinum required in the catalyst layer and increasing the cell efficiency remain important targets for further fuel cell performance gains. Given the detrimental effects of liquid water on cell performance, a major area of interest has been to optimize the water management capabilities of the porous electrode components. This goal, however, demands a deeper understanding of water distribution, transport mechanisms and the overall impact of liquid water on reactant mass transfer inside the PEMFC.

The existence of liquid water in the GDM arises via two main routes: injection and condensation. The first of these occurs when water is generated at the catalyst layer more rapidly than it can be transported through the GDM by gas phase diffusion. This is expected during operation at high humidity and/or high current density conditions which lead to high water generation rates. In this scenario, water emerges from the ionomer phase as a liquid and subsequently flows through the GDM by a capillarity-

controlled invasion percolation process. The second route to liquid water can occur when significant temperature gradients exist across the GDM between the catalyst layer and cooler flow channel. In such instances, water can evaporate in the catalyst layer, but can condense nearer the flow channel where the temperature may drop below the dew point.

The water injection route is relatively straightforward to characterize and has been studied extensively with ex-situ tests on GDMs. An important focus of a number of these studies has been on measuring the conditions (i.e., saturation and capillary pressure) required for breakthrough. Breakthrough occurs when water which has been injected into one face of a GDM is first observed to emerge from the other face. For this state to be reached, a percolating pathway has to have formed through the material. The degree of saturation at breakthrough is of particular interest since gas phase mass transport becomes easier as the amount of liquid water in the media becomes lower. Benziger *et al*.[2] reported a straightforward method to measure breakthrough pressure, but their method to determine GDM saturation by weighing the test specimen after the experiment had difficulty in removing excess water from the sample surface. Büchi *et al*.[3] demonstrated the use of high resolution x-ray tomography to obtain 3D images of liquid water injection into GDMs. This method required very small sample sizes (< 1.5 mm^2) and was subject to finite-size artifacts yielding unreasonably high breakthrough saturations.[4] Recently, we extended our previously reported capillary pressure measurement technique[5] to detect the breakthrough point.[6] Using this method, it was

found that the incorporation of a microporous layer (MPL) on the injection face of the GDM substrate caused a reduction in the breakthrough saturation from 25% to less than 5%. This dramatic reduction was attributed to the elimination of dead-end clusters of water-filled pores in the GDM substrate by the presence of an MPL, an explanation forwarded by several other groups as well.[7, 8] It remains to be demonstrated whether the reduction in saturation due to the MPL observed in *ex-situ* tests also occurs in an operating fuel cell.

Determination of water content in an operating fuel cell remains very difficult to achieve experimentally.[9] Radiography on operating fuel cells using either neutrons or x-rays has been used extensively to study the total water content of an operating fuel cell in-situ. In order to obtain quantitative values of GDM saturation from such measurements, it is necessary to differentiate between (1) water in the flow channels and water in the GDM and (2) water on the cathode and the anode side of the cell. With the exception of a few recent publications, all reported radiography studies have viewed the cell in the through-plane direction, making it impossible to fully address both issues mentioned above. The first of these two questions can be partially answered by counting water only above the rib. Since this approach does not measure the water content in the entire GDM, errors are possible if the saturation above the rib differs considerably from that in other portions of the GDM. Spernjak *et al*.[10] incorporated a transparent flow field to identify liquid water in the flow channel from images and determine the saturation in the GDM alone, but the amount of water in the channel could not be

gauged quantitatively. The second of these issues has been addressed by a number of neutron imaging studies,[11-17] but these generally employed experimental conditions and cell designs that differed significantly from normal fuel cell operation or required assumptions about the water content in certain locations. These limitations can be avoided by examining the cell from the edge, but only a few studies have achieved the required resolution. Hickner *et al*.[18] and Boilliat *et al*.[19] have demonstrated the promise of this approach. The GDM saturations they obtained ranged from 5-10% for the various conditions tested. X-ray radiography of the cell from the edge is another technique that that can yield water saturation. The only studies using this technique were conducted on very dry cells.[20, 21]

The condensation of water in the GDM has only recently begun to receive attention. Neutron imaging studies[18] have revealed water saturation profiles that appear to be significantly affected by condensation.[22] Condensation is an inherently more complex phenomenon than water injection since it depends on many factors including heat conduction and convection, mass transfer, capillarity, nucleation, temperature profiles, etc. Therefore, the study of this phenomenon from either a theoretical or experimental standpoint is much more challenging and has only just begun.[22-24]

The present work aims to study both water invasion and condensation from a unified perspective. A pore network model is developed that simulates both liquid water injection and condensation scenarios described above. The results of pore network

simulations of injection are compared to experimental breakthrough conditions measured for various GDMs with and without MPLs. Condensation is modeled in a simplified way since the main objective is to determine whether it has a significant effect on water saturation and configuration. Finally, this pore network model is used to calculate limiting currents for the various water configuration scenarios.

2. Model Development

Pore network modeling is becoming an increasingly popular approach for studying the GDM in PEMFCs.[1, 8, 25-29] The main advantage of this approach is that it does not require prior knowledge of multiphase transport properties as inputs, as in the case of continuum-based modeling. Instead, it accounts for the specific details of the structure of the porous material in terms of pore and throat elements on a lattice network. Transport of the invading fluid (i.e., water) through the network is governed by relatively simple rules. The use of pore network models is particularly effective for studying the effect of structural parameters of the material or fluid injection conditions on the resulting water configuration, as is exploited in the present work. The model used in this work is an extension of one developed in previously reported work.[1] The main modifications to the model are the inclusion of a microporous layer in the network and the use of an alternative invasion algorithm that better describes breakthrough in thin media. These modifications are discussed in the sections that follow.

2.1. Modeled Domain

The modeled domain in the present study is significantly larger than that used previously.[1] The thickness of the domain is naturally limited by the thickness of the Toray 120 material being modeled in the present case. The thickness of Toray 120 is approximately 390 µm which corresponds to a domain size of 15 pores thick based on a lattice spacing of 25.2 µm between pore centers. The ability to capture the entire

thickness of the material with the pore network model is an important feature since it allows complete simulation of liquid injection and breakthrough processes. In the lateral direction, the domain spans a full 1 mm flow channel and half width of each neighboring rib (also 1 mm), as shown in Figure 1, corresponding to a domain width of 2 mm. Since the domain extends from the center of one rib to another, periodic boundary conditions can be applied on these edges. The domain is also set to 2 mm along the flow channel direction and periodic boundary conditions are applied to these edges as well.

2.2. Gas Phase Mass Transfer

In the present model, mass transport of gas is assumed to occur only by diffusion. It is assumed that the cell is isothermal and fully humidified so that no water vapor pressure gradient exists. Consequently, the gas phase transport in this three-component system (oxygen, nitrogen, water vapor) can be considered to involve oxygen transport through a stagnant layer of nitrogen and water vapor. Oxygen transport can be calculated using Fick's law:

$$n_A = \frac{cD_{A(BC)}}{(1-x_A)}\frac{dx_A}{dl} = cD_{A(BC)}\frac{d\ln(1-x_A)}{dl} \quad \textbf{1}$$

where n_A is the flux of O_2, c is the combined concentration of all gases, x_A is the mole fraction of O_2, l is the transport length and $D_{A(BC)}$ is diffusion coefficient of O_2 through a stagnant mixture of N_2 and H_2O.[30]

To determine the transport through the network, a mass balance is written for each pore *i* using a discretized form of Eq. 1 to describe the steady-state exchange of mass with each neighboring pore *j* as follows:

$$\sum_{j=1}^{n} g_{i-j}\left[ln\left(1-x_{A,i}\right)-ln\left(1-x_{A,j}\right)\right]=0 \quad \textbf{2}$$

where g_{i-j} is the diffusive conductivity of the conduit connecting pore *i* to pore *j*. The conduit is composed of the throat and half the length of each pore *i* and *j*. The total diffusive conductivity g_{i-j} is composed of contributions from the diffusive conductivity of each half-pore *i* ($g_{p,i}$) and *j* ($g_{p,j}$) and the diffusive conductivity of throat *i-j* ($g_{t,i-j}$) as follows:

$$g_{i-j}=\left(\frac{1}{g_{p,i}}+\frac{1}{g_{t,i-j}}+\frac{1}{g_{p,j}}\right)^{-1} \quad \textbf{3}$$

The diffusive conductivity for each half-pore is defined as:

$$g_{p,i}=\frac{A_i c D_{A(BC)}}{L_i}\left(1-S_{W,i}\right) \quad \textbf{4}$$

where A_i, L_i and $S_{W,i}$ are the cross-sectional area, half-pore length and water saturation, respectively, of pore *i*. The presence of liquid water in a conduit is assumed to reduce the gas diffusivity through it to a negligible value. Similarly, the conductivity of throat *i-j* is calculated as:

$$g_{t,i-j}=\frac{A_{i-j} c D_{A(BC)}}{L_{i-j}}\left(1-S_{W,i-j}\right) \quad \textbf{5}$$

where $A_{i\text{-}j}$, $L_{i\text{-}j}$ and $S_{W,i\text{-}j}$ are the cross-sectional area, length and water saturation, respectively, of the throat connecting pores *i* and *j*.

2.3. Microporous Layer

The mean pore size in the MPL is more than an order of magnitude smaller than that in the GDM ($r_{MPL} < 1$ μm whereas $r_{GDM} \approx 10-15$ μm).[31] Thus, for every pore on the face of the GDM, a full pore network model of the MPL would require the use of several thousand nodes on the scale of the pore size of the MPL, as depicted in Figure 2(top). Since this would quickly render the computation intractable for a GDM network of any meaningful size, an alternative approach has been adopted in the present study. Each GDM node at the GDM-MPL interface is connected with a single 'virtual' node in the MPL domain. This virtual node is endowed with a conductivity that reflects the effective behavior of all the individual MPL pores it represents, as shown in Figure 2(bottom). Since this approach essentially treats the MPL using a continuum approximation, details of the water distribution and oxygen concentration profiles in the MPL are lost, but calculation of flux through the MPL becomes straightforward. Determination of the details of the configuration of liquid water flow from the catalyst layer through the MPL and into the GDM is also not possible with this approach since MPL pore scale events are not resolved. To circumvent this limitation for simulations of injections into GDMs with an MPL, the present study makes use of findings from a previous study[6] which considered that water emerges from the MPL at a single point and enters the GDM from

a single pore at the GDM-MPL interface. The injection point is always set to be at the center of the domain. It should also be noted that the MPL is assumed to penetrate into the GDM a distance equivalent to one layer of pores (25.2 µm in the present case). Thus, a GDM that is 15 pores thick without an MPL is converted to a structure made up of a 14-pore thick GDM and a 1-layer thick MPL of arbitrary thickness.

To calculate the gas phase diffusive transport through the MPL, the conductivity of a virtual node is calculated as:

$$g_{mpl,i} = \frac{A_i c D_{A(BC)}}{L_i} \frac{\varepsilon}{\tau} \qquad \textbf{6}$$

where ε is the MPL porosity, taken to be 0.7[31] and τ is the tortuosity calculated using the Bruggeman relation[32] ($\tau = \varepsilon^{-0.5}$). The thickness of the MPL is set to 50 µm. The area A_i for transport through the MPL in the through-plane direction is set equal to the square of lattice constant while the area for transport along the MPL in the in-plane direction is given by the product of the lattice constant and the MPL thickness. In this way, the MPL is represented by a single layer of nodes although its thickness can be adjusted independently of the lattice constant. The transport length L_i between the MPL nodes similarly depends on the direction. The length is the MPL thickness in the z-direction and half the lattice constant in the x and y directions. For transport from a GDM pore into the MPL, Eq. 6 is substituted into Eq. 3 to calculate the conductivity of a pore-throat-MPL node conduit yielding:

$$g_{p,i-mpl} = \left(\frac{1}{g_{p,i}} + \frac{1}{g_{t,i}} + \frac{1}{g_{mpl,j}} \right)^{-1} \quad \textbf{7}$$

The conductivity for transport between two MPL nodes is calculated as:

$$g_{mpl,i-mpl,j} = \left(\frac{1}{g_{mpl,i}} + \frac{1}{g_{mpl,j}} \right)^{-1} \quad \textbf{8}$$

The throat connect two MPL nodes is of negligible length so offers no transport resistance.

2.4. Water Distribution Algorithms

2.4.1. Invasion Percolation

In our previous model,[1] water was distributed in the pore network according to access-limited ordinary percolation (ALOP).[33] According to this approach, the capillary pressure is increased step-wise. At each step, all pores that are both penetrable at the specified pressure and connected to the source of invading fluid either directly or via a pathway of invaded pores become filled. This algorithm describes pressure-controlled capillary pressure experiments very well, but is not ideally suited to simulating breakthrough in fuel cell electrodes. In this work, we use an alternative algorithm termed invasion percolation (IP) presented by Wilkinson and Willemsen.[34] In the IP algorithm, water enters the sample from a predefined injection source (*i.e.* CL-GDM interface) and is therefore also access-limited. Instead of increasing the applied pressure step-wise,

however, each step of the IP proceeds by filling the most easily penetrable pore that is accessible. After a pore is invaded, a number of new pores are made accessible and become candidates for penetration in the next step. At every step the most easily penetrable accessible pore is filled next. The algorithm continues until a throat on the outlet face over the flow channel is invaded, corresponding to the breakthrough point. The simulation is stopped at breakthrough since the injection rates occurring in fuel cells are capillary-dominated with a low viscosity ratio[29] so that once a percolating path is formed the relative permeability is automatically high enough to support the flow rate without the penetration of any additional pores.[35]

The main difference between the two percolation algorithms is that the IP resolves the sequence in which individual pores are filled, while ALOP fills all accessible pores simultaneously. ALOP is favored for reasons of computational economy, but IP is better suited to simulations in thin media where percolation can occur before the typically observed percolation threshold. IP allows the precise determination of the sample saturation required for a percolating path to form and breakthrough to be reached. The specifics of percolation properties in thin GDMs have been discussed elsewhere.[4]

2.4.2. Condensation Algorithm

In this study, condensation is considered to occur under isothermal conditions without the effects of heat transfer or mass transfer of water vapor. The rationale for basing the simulations on this simplified model is presented at the end of this sub-section. The

model is based on a percolation approach to approximate the configuration of liquid water resulting from cluster growth at isolated nucleation sites and subsequent coalescence and percolation of growing clusters. This simplified approach begins by assuming condensation commences over the cool flow field rib areas[24] and randomly assigns a small fraction (arbitrarily chosen as 10%) of the pore throats in this region as nucleation sites. Invasion percolation (IP) described in the previous section proceeds from each nucleation site simultaneously in a manner similar to the invasion from the CL-GDM injection face. In order to simulate condensation, it is necessary to track the individual water clusters extending from each nucleation site to determine when each achieves breakthrough. When a given cluster achieves breakthrough, its growth is stopped since any further water joining this cluster by condensation would increase flow out the breakthrough site, but not cause the cluster to grow. Similarly, if a cluster grows to join another that has already achieved breakthrough, then the growth of the former will cease for the same reason. On the other hand, two clusters that have not reached breakthrough but grow to join each other simply coalesce into a single cluster capable of continued growth. The algorithm proceeds until all the clusters emanating from the randomly seeded nucleation sites either achieve breakthrough or coalesce with other clusters that have done so. This signifies the point when all condensing water has established a path to the GDM outlet and no further growth occurs.

Obviously, this approach does not rigorously describe the phenomena associated with phase change within the GDM, such as the influence of latent heat on temperature

gradients, limitations of heat and mass transport rates to and from the condensed water clusters and the competing effects of water evaporation in regions of sub-saturated vapor. The compression of the GDM under the rib, which would tend to promote cluster growth in more easily invaded uncompressed areas[36] over the land and hence earlier breakout of growing water clusters, is also neglected. In fact, the simplifications made here all tend to increase the amount of liquid water that would form above the land and so describe a situation in which condensation would have its largest possible effect. The primary objective in considering condensation here is to determine whether GDM water configurations likely due to condensation can help explain the experimentally observed limiting current densities. If the simplified algorithm yields results similar to the experimental observations, then closer examination of condensation using a more sophisticated algorithm is warranted.

3. Experimental

3.1. Breakthrough Point by Capillary Pressure Measurement

The water-air capillary method employed here was adapted from a previously described technique[5] to measure the breakthrough capillary pressure and saturation.[6] Briefly, this method detects the point of water breakthrough by measuring the capillary pressure P_C as a function of saturation of a 2-layer sample consisting of a GDM and a dry hydrophilic membrane. Water enters the 2-layer stack from the bottom face of the GDM. The capillary pressure then is the difference between the liquid pressure on the bottom and the gas pressure at the top, *i.e.* $P_C = P_L - P_G$. As P_C is increased by reducing the gas pressure in the sample, liquid water invades an increasingly larger volume of the GDM. When water breakthrough of the GDM occurs, rapid wicking of water into the dry hydrophilic membrane occurs and is easily detectable by measuring the variation of the amount of water uptake with time.[6] The experiment is terminated once breakthrough occurs. Prior to breakthrough this method provides valid measurements of points on the GDM capillary pressure curve. All tests were conducted at room temperature since the balance and syringe pump used could not withstand elevated temperatures.

3.2. Breakthrough Point by Direct Water Injection

An alternative means to measure the water breakthrough point is to inject water into the GDM at a constant rate and observe the emergence of water from the sample outlet

face. Similar experiments have been conducted by other workers[37-39], but in none of those cases was the water saturation at breakthrough reported. The experimental setup used for in the present tests is shown in Figure 3. The sample is mounted firmly between two plates and water is injected from above. The rate of water injection is chosen to match the amount of water produced in a fuel cell operating at 1 A/cm^2. For the 19.05 mm diameter samples used here, this corresponds to a flow rate of 16 mL/min. Care is taken during setup and priming of the system to ensure that the connections are free of gas bubbles. This assures that all water injected into the system enters the GDM rather than compressing bubbles. It is also possible that the sample could flex slightly due to the applied water pressure and this would give the appearance of additional water uptake in the sample. This is probably not significant in the Toray 120 sample tested here however, which is very stiff and thick. Assuming the system is free of bubbles and the sample does not flex significantly, the GDM saturation can be found from the product of the syringe pump rate and time elapsed from the start of the experiment. Prior to the start of the experiment, a vent on the sample holder is kept open to allow water to escape when the syringe pump is initiated. Closing of the vent starts the experiment by forcing water to flow through the GDM sample. This causes a sharp rise in the liquid pressure response P_L, as can been seen in Figure 4, which allows easy detection of the instant water injection into the sample begins.

An analytical balance is positioned below the sample to catch emerging water droplets. This not only allows detection of the breakthrough point, but also enables the water

holdup in the GDM to be tracked over time. The amount of water in the GDM at any time can be found from the difference between the known amount of water injected into the sample and the mass of water collected in the weighing pan. Figure 4 shows a plot of the variation of the GDM water saturation with time obtained in this way. The saw-tooth behavior of the response is due to the fact that water emerges from the GDM in discrete droplets. A decrease in the GDM saturation corresponds to a water droplet detaching from the GDM surface and falling into the collection pan on the balance. This approach counts the liquid water volume of a droplet hanging from the GDM surface as part of the saturation although it is not contributing to water volume inside the GDM. This error increases as the droplet grows, but is corrected when the droplet detaches and is registered by the balance. Since each minimum in the saw-tooth curve in Figure 4 corresponds to detachment of a droplet, only the saturation values at these points are used to generate the saturation-capillary pressure curves. Evaporation of water from the collection pan during each test is prevented by filling the pan with a layer of non-volatile oil prior to the start of the experiment. As water drops into the pan, it sinks below the oil so that it is not exposed to the air.

The process of droplet growth, emergence and detachment is responsible for the saw-tooth behavior of the pressure trace after the initial breakthrough ($t > 50$ s) in Figure 4. When a droplet appears at the GDM surface, the pressure reaches a peak before decaying as the droplet grows. This is expected since the capillary pressure throughout the system decreases as the droplet becomes larger and its radius of curvature increases.

When the droplet detaches, the pressure begins to rise again. While the pressure is rising, no droplet is visible presumably since the advancing air-water interface is still inside the GDM. The increase in pressure is presumably required to re-establish the pathway to the outlet pore, suggesting that the droplet carries with it water from inside the sample as it detaches. A more detailed study of the relation between droplet detachment, pressure response and PTFE content was not carried out here.

One of the main difficulties with this technique is that liquid water can emerge at the edge of the GDM and attach to the wall of the sample holder. This effect is likely due to inadvertent compression and crushing of the sample during mounting. The breakthrough pressure and saturation measurements obtained in tests when this occurs do not reflect the true behavior of the material and are disregarded. Only successful experiments where this phenomenon does not occur are reported here as a confirmation of the modified capillary pressure approach described in Section 3.1. All tests in the present work were conducted at room temperature due to the delicate nature of the equipment (balance and syringe pump). It is conceivable, however, that in the future this test could be adapted to high temperature, for instance, by heating the sample holder. The ability to study breakthrough at temperatures relevant to PEMFC operation would be highly desirable.

3.3. GDM Materials

The properties of the GDM materials tested are listed in Table 1. Toray GDMs of two

different thicknesses (Toray 060 and Toray 120) have been tested, each with (Toray 060C, Toray 060D, Toray 120C) and without (Toray 060A, Toray 120A) PTFE treatment. Also relevant to the present study are breakthrough results previously reported[6] for SGL 10 series materials with (SGL 10BB) and without (SGL 10BA) an MPL. Both of the SGL materials have identical PTFE-treated fibrous substrates.

4. Results and Discussion

4.1. Experimental Determination of GDM Breakthrough Conditions

Breakthrough conditions have been measured experimentally for various GDMs with differing thickness and PTFE loading using the two independent techniques described in Section 3. Figure 5 shows the results of the breakthrough experiments obtained for Toray 120 (left) and Toray 060 (right) along with the full capillary pressure curves for the same samples obtained from a previous study.[36] Breakthrough saturations of 0.33 and 0.41 are obtained in Toray 120A and 060A, respectively, that do not contain PTFE, whereas values of 0.14 and 0.20 are measured in Toray 120C and 060C, respectively, that have been treated with PTFE. Also shown in Figure 5(left) is the breakthrough point for Toray 120C obtained using the direct injection method and this measurement agrees closely with that obtained by the capillary pressure measurement. Notably the presence of PTFE reduces the breakthrough saturation by about half in both the thin (Toray 060) and thick (Toray 120) materials.

The data obtained by the modified capillary pressure method prior to breakthrough as described in Section 3.1 also provide useful information. The curves obtained for the thick Toray 120 samples by the regular (from our previous study) and modified methods agree very well with each other. In the case of the thinner Toray 060 samples, the curves are in qualitative agreement but some noticeable discrepancies exist. This is not surprising since the thinner samples have less pore volume and therefore the effect of

random differences in the porosity of samples will be more significant. Differences in thickness also explain why the breakthrough pressures for the thin Toray 060 samples are somewhat lower than the thicker Toray 120 samples. In a thinner medium, a percolating path can be formed at lower pressures since it is statistically more likely that any given path will span the sample. Consider, for example, the extreme case of a media consisting of only a single layer of pores. Water entry into the largest and most easily penetrable pore will result in immediate breakthrough at the lowest possible pressure. As the material becomes thicker, it becomes more likely that a given path will encounter a constriction (resulting in a dead end cluster) before spanning the sample and therefore require a higher overall breakthrough pressure. Operation of a fuel cell with thinner GDMs may be a useful cell design feature since a lower injection capillary pressure would imply less back-pressure to the catalyst layer and therefore lower saturation there.

Another interesting feature of the breakthrough points shown in Figure 5 is that the addition of PTFE does not alter the breakthrough pressure for Toray samples with the same thickness. Benziger *et al*.[2] have reported an increase in breakthrough pressure due to the addition of PTFE. This discrepancy could be due to differences in samples and PTFE application. Also, in this earlier study, sufficient time may not have been allowed for water to reach equilibrium at each step before the water pressure was increased for the next step. In any event, a more complete study of breakthrough conditions in a wide range of materials is needed to fully understand the effect of PTFE and to find loadings and application techniques that minimize breakthrough pressure and saturation.

4.2. Pore Network Simulations of Water Injection

In order to simulate the effect of liquid water on fuel cell performance, it is necessary to first calculate realistic liquid water distributions in the GDM. Water injection into identical realizations of the GDM with and without an MPL has been simulated in the pore network using the IP algorithm. The modeled domains for the cases where MPL is absent and present are shown in Figure 1(left) and Figure 1(right), respectively. Once the breakthrough configuration of water has been obtained, mass transfer-limited currents are calculated in the partially saturated networks.

The simulated oxygen concentration and liquid water distribution within the GDM can be visualized along planar slices normal to the z-direction from the flow channel to the catalyst layer. Figure 6 presents the layout of the slices shown subsequently in Figure 7, Figure 9 and Figure 11. As one advances from left to right beginning with the panel at the top left and then progresses to the row beneath, the slices progressively move from the plane along the flow channel and land toward the plane of the catalyst layer. Figure 7 shows the oxygen and liquid water distributions in the GDM without MPL in each of these planes when water is injected from the catalyst layer. The color scale denotes the oxygen concentration ranging from $x_{O_2} = 0$ (dark blue) to $x_{O_2} \approx 0.1$ (dark red), while the black nodes represent pores filled with liquid water. When no MPL is present, liquid water is able to invade the GDM from any location along the GDM-CL interface so that many liquid clusters are formed over the entire interface (bottom right panel of Figure 7). However, most of these clusters lead to dead-ends and only a single point of

breakthrough is observed at the GDM-channel interface (second panel from the left along the top row). The water saturation within the entire GDM when breakthrough is reached in this case is determined to be S_W = 0.11. This water saturation is in reasonable agreement with the experimentally measured breakthrough saturation value of about 0.14 for Toray 120C. The water saturation profiles through the thickness of the GDM with no MPL are shown in Figure 8(left). As expected, the profile for the injection case (*i.e.* curve GDM_I) exhibits a high saturation at the GDM-CL interface that decays rapidly and reaches nearly zero at the GDM-channel interface where breakthrough occurs at a single isolated location.

When an MPL exists between the catalyst layer and the GDM, water emerges from the MPL at a single isolated location[6-8] similar to the way single water droplets emerge from the GDM at the GDM-flow channel interface.[38, 40] Liquid water injection into the GDM from a point-source leads to a much different liquid water configuration as can be seen in Figure 9, where the number of dead-end clusters is reduced greatly and the overall water saturation S_W at breakthrough is only 0.04. Experimental measurement of the breakthrough saturation for Toray 120C with an MPL has not been performed, but the addition of an MPL to SGL 10BA has been experimentally shown to reduce saturation to almost negligible values ($S_W \approx 0.04$).[6] The profile shown in Figure 8(right) for injection into a GDM with an MPL (curve GDM_MPL_I) indicates that the saturation remains low everywhere within the GDM and never exceeds 0.08 at any location.

Calculations have also been carried out to compare the limiting current for the network with an MPL to the value obtained for the network without an MPL once the breakthrough water configurations are established. Figure 10 shows the calculated limiting current versus the water saturation for each GDM and MPL combination. The marked reduction in water saturation in the GDM-MPL system leads to a 20% improvement in the limiting current density to a value of 2.8 A/cm^2 from the value of 2.35 A/cm^2 obtained for the GDM without an MPL. Although an improvement of 20% is in accord with experimental observations,[41-44] the magnitude of these computed limiting current densities are unrealistically high. In a previous study,[1] the same pore network model showed that a water saturation of about 30% is sufficient to reduce the limiting current density to typically observed values of 1 - 1.5 A/cm^2. However, the conditions of liquid water breakthrough were not closely considered in that study. The high limiting currents obtained in the present simulations are presumably due to (1) the low water saturations arising from injection and/or (2) the neglect of mass transfer resistances within the catalyst layer in the current version of the model. In an effort to understand the high value of limiting current calculated here, the possibility that condensation contributes additional water to the GDM beyond that resulting from injection alone is explored further in the next section. The inclusion in the model of mass transfer resistances associated with the catalyst layer remains a subject for future work.

4.3. Pore Network Simulations of Condensation

As shown in the previous section, the IP algorithm yields water saturation values at

breakthrough in good agreement with those determined experimentally both with and without an MPL present. Subsequent calculations based on gas phase mass transfer predict limiting currents that are unrealistically high. Our objective now is to determine if the generation of liquid water in the GDM due to a condensation-type mechanism leads to higher water saturation levels and therefore lower, more realistic limiting current densities typical of operating fuel cells. As discussed in section 2.4.2, the condensation algorithm considered is relatively simple. The water configurations arising from condensation are generated by assuming water condensation will commence under the channel rib, following by cluster growth as described in Section 2.4.2. The intention of this simplified approach is to estimate the possible impact that liquid water condensation and accumulation under the channel ribs could have on PEMFC performance.

The distributions of oxygen and liquid water predicted by the condensation algorithm described in Section 2.4.2 are shown in Figure 11 for a GDM with no MPL. The water saturation and the limiting current density at breakthrough are determined to be 9.5% and 2.44 A/cm^2, respectively. Since the invasion and cluster growth occurs in the coolest region over the channel ribs (see panels in top row of Figure 11), the presence of an MPL has no influence on the resulting water configuration, although it reduces the limiting current density slightly to 2.38 A/cm^2 due to the added mass transfer resistance of the MPL. As can be seen in Figure 8, the liquid water saturation profiles predicted by the condensation algorithm are identical irrespective of the presence (curve GDM_MPL_C)

or absence (curve GDM_C) of MPL. As with the previous algorithm, however, the predicted limiting current is still higher than that observed in operating fuel cells, suggesting that condensation alone does not distribute liquid water into the GDM in such a way to significantly impede mass transfer in the GDM itself. Also, it is interesting to note that an MPL has little effect on the water configuration during condensation since water clusters form on the flow field side of the domain. Thus, if condensation were the only mechanism by which liquid water forms in the GDM, then these results suggest that a fuel cell with an MPL should show little performance advantage at high current density operation, at odds with experimental observations.[41-44]

4.4. Pore Network Simulations of Simultaneous Condensation and Injection

An alternative possibility is that injection and condensation occur simultaneously. It is beyond the scope of the present work to calculate the complex non-isothermal effects necessary for this to occur. It is, however, a relatively simple matter to combine the injection and condensation algorithms to approximate the water configuration that might result from such a situation. In this scenario, the invading water clusters emanate from both the nucleation sites over the channel ribs and the catalyst layer-GDM interface. The same rules governing cluster coalescence and breakthrough adopted for the condensation algorithm alone apply in this case as well. The resulting water saturation profiles shown in Figure 8 (curves GDM_CI and GDM_MPL_CI) are essentially a superposition of the injection and condensation simulations. The overall saturation and limiting current density at breakthrough are 16% and 2.01 A/cm^2, respectively, for

the GDM without an MPL and 10.4% and 2.3 A/cm^2 when an MPL is present. The additional water predicted by the combined injection-condensation mechanism reduces the limiting current, although it is still somewhat high. This suggests that the effect of mass transfer resistance in the catalyst layer must also be included to bring the model predictions in closer agreement with experimentally observed fuel cell behavior. The limiting current density is likely determined by factors other than the average saturation in the GDM at breakthrough. It is difficult to confirm whether the water saturation values calculated using the present model are representative of operating fuel cells since in-situ determination of GDM saturation is very challenging.[9, 45] Unlike the other scenarios investigated, the water saturation decreases to a minimum near the center of the GDM for the case with no MPL (Figure 8(left)). A similar minimum in the water saturation profile has previously been reported by Hickner *et al*.[18] from neutron imaging experiments providing some support that simultaneous injection-condensation plays a role, although it must be conceded that Hickner *et al*.[18] used GDMs with MPLs in their setup.

5. Conclusions

The present work aims to simulate realistic water configurations generated within GDMs on the basis of a pore network model. The model is able to reproduce the experimental injection breakthrough saturations and has been extended to describe water condensation. Finally, the case of simultaneous water injection and condensation was simulated. In all cases, the predicted limiting currents are unreasonably high. Since the calculated liquid water configurations appear to be fairly realistic, the saturation levels at breakthrough agree well with those observed in *ex-situ* experiments and the GDM saturation agree quantitatively with the neutron imaging results of Hickner *et al*.,[18] the neglect of catalyst layer mass transfer resistance in the model is likely responsible for its failure to accurately predict the limiting current. This question should be addressed in future work. Condensation of liquid water in the present model was approximated by assuming that it occurs under the channel ribs since the aim was to determine the maximum impact that condensation could have on oxygen mass transfer in the GDM. Development of a pore network model that includes the effects of heat transfer and water vapor mass transfer is necessary to provide a complete description of condensation and evaporation in the GDM.

Another important issue that was not addressed in the present work is the effect that elevated temperature may have on capillary properties of these materials. All experimental breakthrough tests were conducted at room temperature although fuel

cells operate at temperatures of 80 ^{o}C or more. Since contact angle is a complex function of temperature[46] it is possible that the wettability and breakthrough conditions will be altered in an operating fuel cell.[47] The experimental study of breakthrough conditions at higher temperatures will be crucial to more fully understand the impact of GDM water saturation on PEMFC performance.

Acknowledgments

The authors wish to thank the Natural Science and Engineering Research Council of Canada (NSERC) for financial support throughout the course of this project.

References

1. J. T. Gostick, M. A. Ioannidis, M. W. Fowler and M. D. Pritzker, *J. Power Sources*, **173**, 277 (2007).
2. J. Benziger, J. Nehlsen, D. Blackwell, T. Brennan and J. Itescu, *J. Membrane Sci.*, **261**, 98 (2005).
3. F. N. Büchi, R. Flückiger, D. Tehlar, F. Marnoe and M. Stampanoni, *ECS Transactions*, **16**, 587 (2008).
4. J. T. Gostick, M. A. Ioannidis, M. W. Fowler and M. D. Pritzker, in *Modern Aspects of Electrochemistry*, C. Y. Wang and U. Pasaogullari Editors, Springer, Berlin (In Press).
5. J. T. Gostick, M. A. Ioannidis, M. W. Fowler and M. D. Pritzker, *Electrochem. Commun.*, **10**, 1520 (2008).
6. J. T. Gostick, M. A. Ioannidis, M. W. Fowler and M. D. Pritzker, *Electrochem. Commun.*, **11**, 576 (2009).
7. J. H. Nam, K.-J. Lee, G.-S. Hwang, C.-J. Kim and M. Kaviany, *Int. J. Heat Mass Transfer*, **52**, 2779 (2009).
8. M. Rebai and M. Prat, *J. Power Sources*, **192**, 534 (2009).
9. J. St Pierre, *J. Electrochem. Soc.*, **154**, B724 (2007).
10. D. Spernjak, S. G. Advani and A. K. Prasad, *J. Electrochem. Soc.*, **156**, B109 (2009).
11. D. Kramer, J. Zhang, R. Shimoi, E. Lehmann, A. Wokaun, K. Shinohara and G. G. Scherer, *Electrochim. Acta*, **50**, 2603 (2005).
12. J. Zhang, D. Kramer, R. Shimoi, Y. Ono, E. Lehmann, A. Wokaun, K. Shinohara and G. G. Scherer, *Electrochim. Acta*, **51**, 2715 (2006).
13. J. P. Owejan, T. A. Trabold, D. L. Jacobson, M. Arif and S. G. Kandlikar, *Int. J. Hydrogen Energy*, **32**, 4489 (2007).
14. Y. S. Chen and H. Peng, *J. Fuel Cell Sci. Tech.*, **6**, 031016.1 (2009).
15. Y.-S. Chen, H. Peng, D. S. Hussey, D. L. Jacobson, D. T. Tran, T. Abdel-Baset and M. Biernacki, *J. Power Sources*, **170**, 376 (2007).
16. A. Turhan, K. Heller, J. S. Brenizer and M. M. Mench, *J. Power Sources*, **180**, 773 (2008).
17. J. J. Kowal, A. Turhan, K. Heller, J. Brenizer and M. M. Mench, *J. Electrochem. Soc.*, **153**, A1971 (2006).
18. M. A. Hickner, N. P. Siegel, K. S. Chen, D. S. Hussey, D. L. Jacobson and M. Arif, *J. Electrochem. Soc.*, **155**, B427 (2008).
19. P. Boillat, D. Kramer, B. C. Seyfang, G. Frei, E. Lehmann, G. G. Scherer, A. Wokaun, Y. Ichikawa, Y. Tasaki and K. Shinohara, *Electrochem. Commun.*, **10**, 546 (2008).
20. C. Hartnig, I. Manke, R. Kuhn, N. Kardjilov, J. Banhart and W. Lehnert, *Appl. Phys. Lett.*, **92**, 134106 (2008).
21. C. Hartnig, I. Manke, R. Kuhn, S. Kleinau, J. Goebbels and J. Banhart, *J. Power Sources*, **188**, 468 (2009).
22. A. Z. Weber and M. A. Hickner, *Electrochim. Acta*, **53**, 7668 (2008).

23. S. Kim and M. M. Mench, *J. Electrochem. Soc.*, **156**, B353 (2009).
24. S. Basu, C. Y. Wang and C. K. Chen, *J. Electrochem. Soc.*, **156**, B748 (2009).
25. K.-J. Lee, J. H. Nam and C.-J. Kim, *Electrochim. Acta*, **54**, 1166 (2009).
26. K.-J. Lee, J. H. Nam and C.-J. Kim, *J. Power Sources*, **195**, 130 (2009).
27. L. Ceballos and M. Prat, *J. Power Sources*, **195**, 825 (2010).
28. P. K. Sinha and C. Y. Wang, *Chem. Eng. Sci.*, **63**, 1081 (2008).
29. P. K. Sinha and C. Y. Wang, *Electrochim. Acta*, **52**, 7936 (2007).
30. C. R. Wilke, *Chem. Eng. Prog.*, **46** 95 (1950).
31. J. T. Gostick, M. W. Fowler, M. A. Ioannidis, M. D. Pritzker, Y. M. Volfkovich and A. Sakars, *J. Power Sources*, **156**, 375 (2006).
32. J. van Brakel and P. M. Heertjes, *Int. J. Heat Mass Transfer*, **17**, 1093 (1974).
33. F. A. L. Dullien, *Porous Media: Fluid Transport and Pore Structure*, Academic Press, New York (1992).
34. D. Wilkinson and J. F. Willemsen, *J. Phys. A: Math. Gen.*, **16**, 3365 (1983).
35. R. Lenormand, *J. Phys.-Condes. Matter*, **2**, SA79 (1990).
36. J. T. Gostick, M. A. Ioannidis, M. W. Fowler and M. D. Pritzker, *J. Power Sources*, **194**, 433 (2009).
37. A. Bazylak, D. Sinton and N. Djilali, *J. Power Sources*, **176**, 240 (2008).
38. S. Litster, D. Sinton and N. Djilali, *J. Power Sources*, **154**, 95 (2006).
39. B. Gao, T. S. Steenhuis, Y. Zevi, J. Y. Parlange, R. N. Carter and T. A. Trabold, *J. Power Sources*, **190**, 493 (2009).
40. X. G. Yang, F. Y. Zhang, A. L. Lubawy and C. Y. Wang, *Electrochem. Solid-State Lett.*, **7**, A408 (2004).
41. S. Park, J. W. Lee and B. N. Popov, *J. Power Sources*, **163**, 357 (2006).
42. K. Karan, H. Atiyeh, A. Phoenix, E. Halliop, J. G. Pharoah and B. Peppley, *Electrochem. Solid-State Lett.*, **10** B34 (2007).
43. D. Malevich, E. Halliop, B. A. Peppley, J. G. Pharoah and K. Karan, *J. Electrochem. Soc.*, **156**, B216 (2009).
44. R. P. Ramasamy, E. C. Kumbur, M. M. Mench, W. Liu, D. Moore and M. Murthy, *Int. J. Hydrogen Energy*, **33**, 3351 (2008).
45. A. Bazylak, *Int. J. Hydrogen Energy*, **34**, 3845 (2009).
46. A. W. Neumann and W. Tanner, *J. Colloid Interface Sci.*, **34**, 1 (1970).
47. C. Lim and C. Y. Wang, *Electrochim. Acta*, **49**, 4149 (2004).

Nomenclature

Symbol	Name	Units
A	Area for transport	m^2
c	Gas Concentration	$mol \cdot m^{-3}$
D_{ij}	Diffusion Coefficient	$m^2 \cdot s^{-1}$
δ	GDM Thickness	m
ε	Porosity	-/-
g	Diffusive Conductivity	$mol \cdot s^{-1}$
L	Pore or throat Length	m
l	Transport Length	m
n_i	Molar Flux of Species i	$mol \cdot m^{-2} \cdot s^{-1}$
P_C	Capillary Pressure, defined as $P_L - P_G$	Pa
P_G	Liquid Pressure	Pa
P_L	Gas Pressure	Pa
r	Pore Radius	m
S_w	Water Saturation	-/-
t	Time	s
τ	Tortuosity	-/-
x	Mole Fraction	-/-

Figures and Tables

Table 1: Properties of GDMs tested

Sample Name	Thickness [um]	Porosity	PTFE Loading [wt%]
Toray 120A	390	0.78	0
Toray 120C	390	0.75	10
Toray 060A	220	0.78	0
Toray 060C	220	0.75	10
Toray 060D	220	0.72	20
SGL 10BA	380	0.88	5
SGL 10BB	420	0.84	5*

* PTFE loading in fibrous substrate, which is identical to SGL 10BA

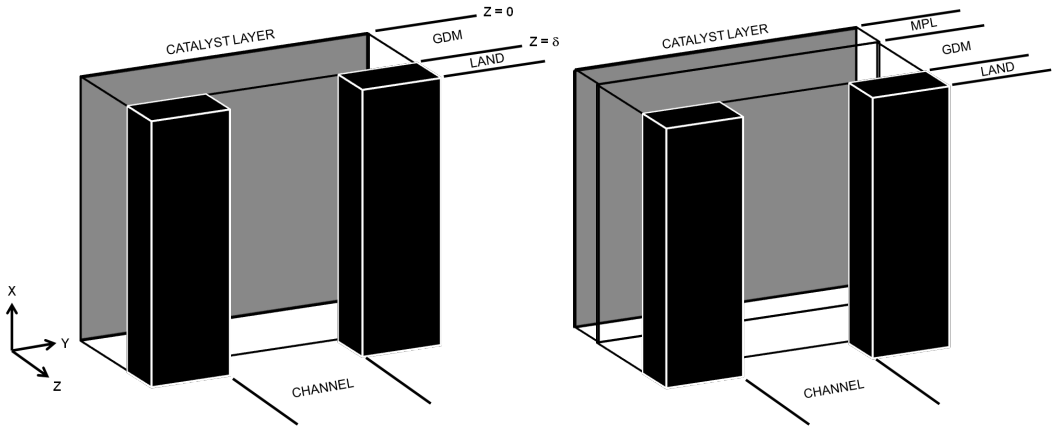

Figure 1: Schematic diagram of modeled domain without microporous layer (left) and with microporous layer (right).

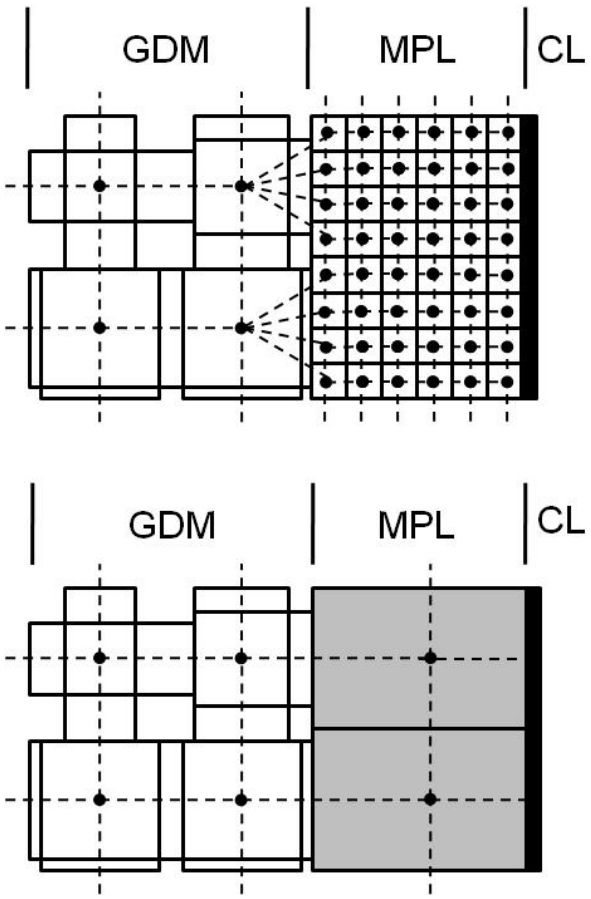

Figure 2: Schematic description of pore network construction. (Top) GDM interfacing with a fully explicit pore network description of the MPL. (Bottom) GDM interfacing with a simplified description of the MPL containing virtual or effective nodes denoted by grey regions.

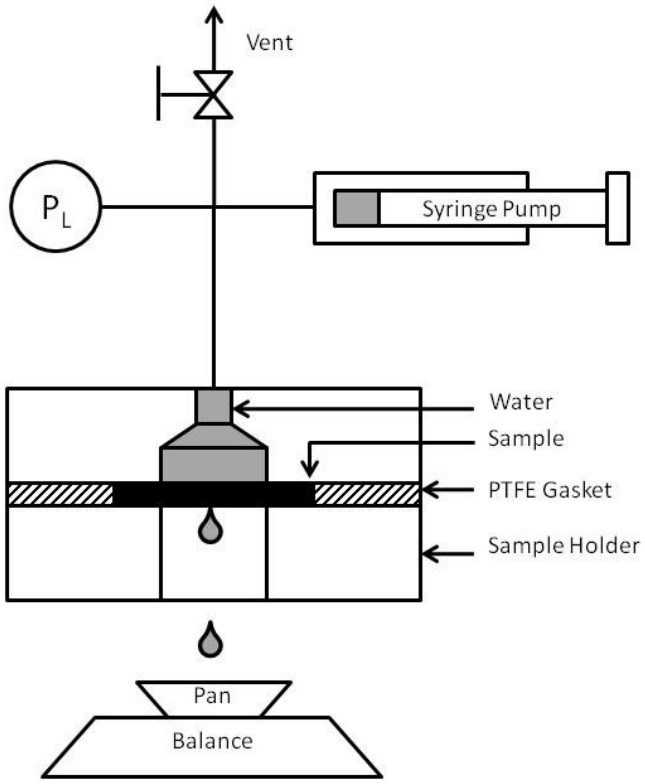

Figure 3: Schematic diagram of water injection experimental setup

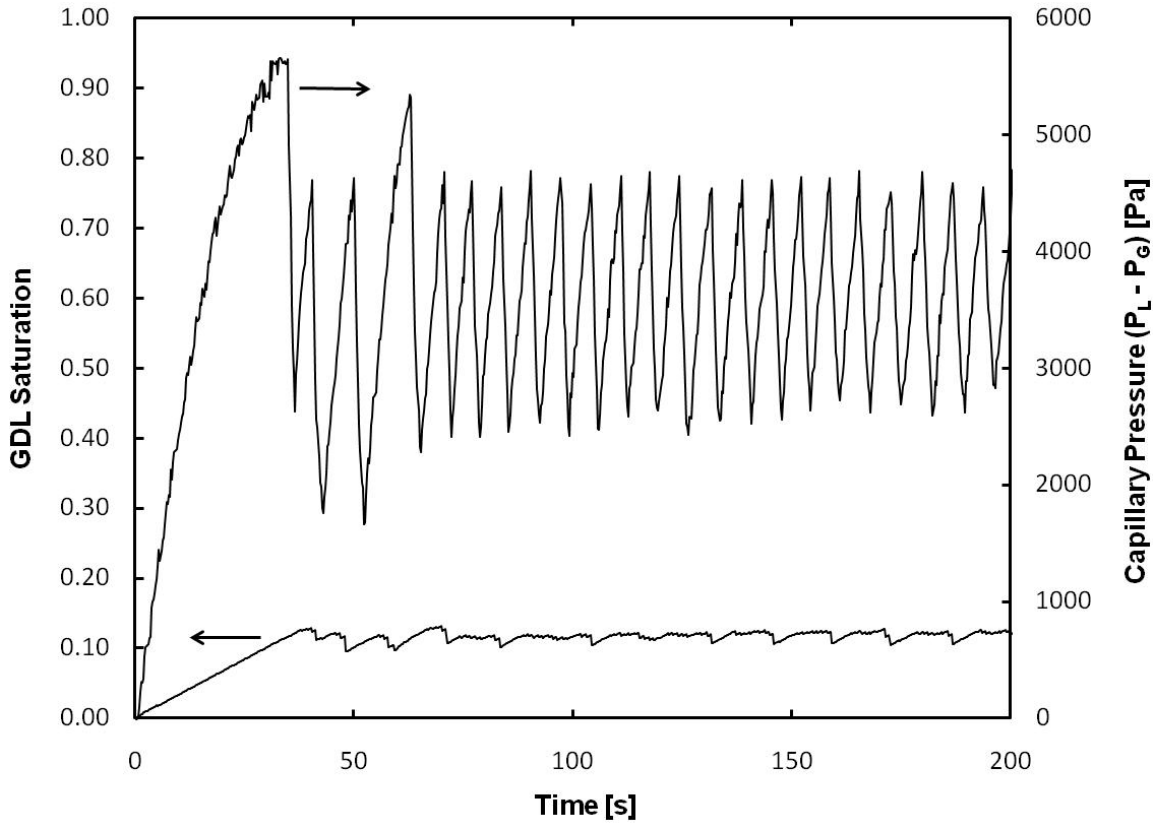

Figure 4: Typical evolution of capillary pressure and water saturation obtained during experiment using the positive displacement injection method on Toray 120C GDM.

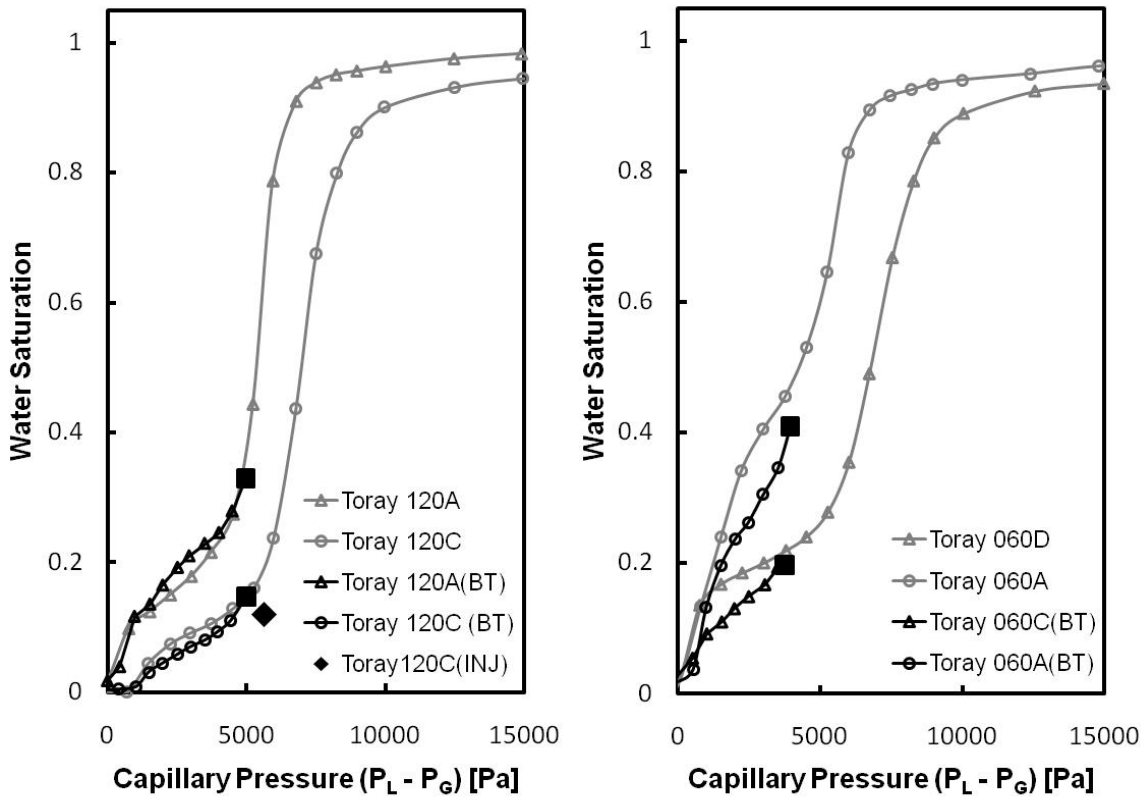

Figure 5: Breakthrough test on Toray 120 (left) and Toray 060 (right) with (circle markers) and without (triangle markers) PTFE coating. Breakthrough points determined by the modified capillary pressure method (BT) are marked with a large black square at the termination of each breakthrough experiment. The large black diamond indicates the breakthrough point determined by the injection experiment (INJ). Full capillary pressure curve data (grey lines and markers) are taken from Gostick *et al*.[36]

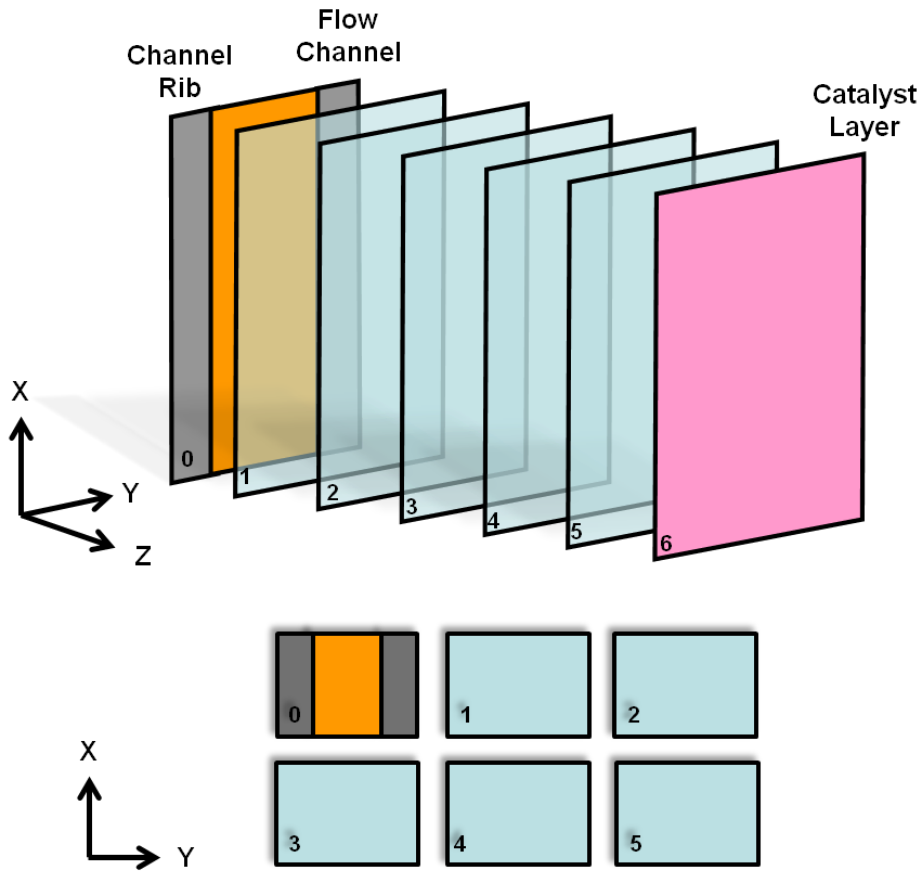

Figure 6: Layout of panels showing the sequence of planar slices presented in Figure 7, Figure 9 and Figure 11. As panels are read from left to right in each row, the corresponding planar slices progress from the channel rib-flow channel layer to the catalyst layer. Not shown is the panel for the catalyst layer where the concentration is uniformly zero due to limiting current assumption.

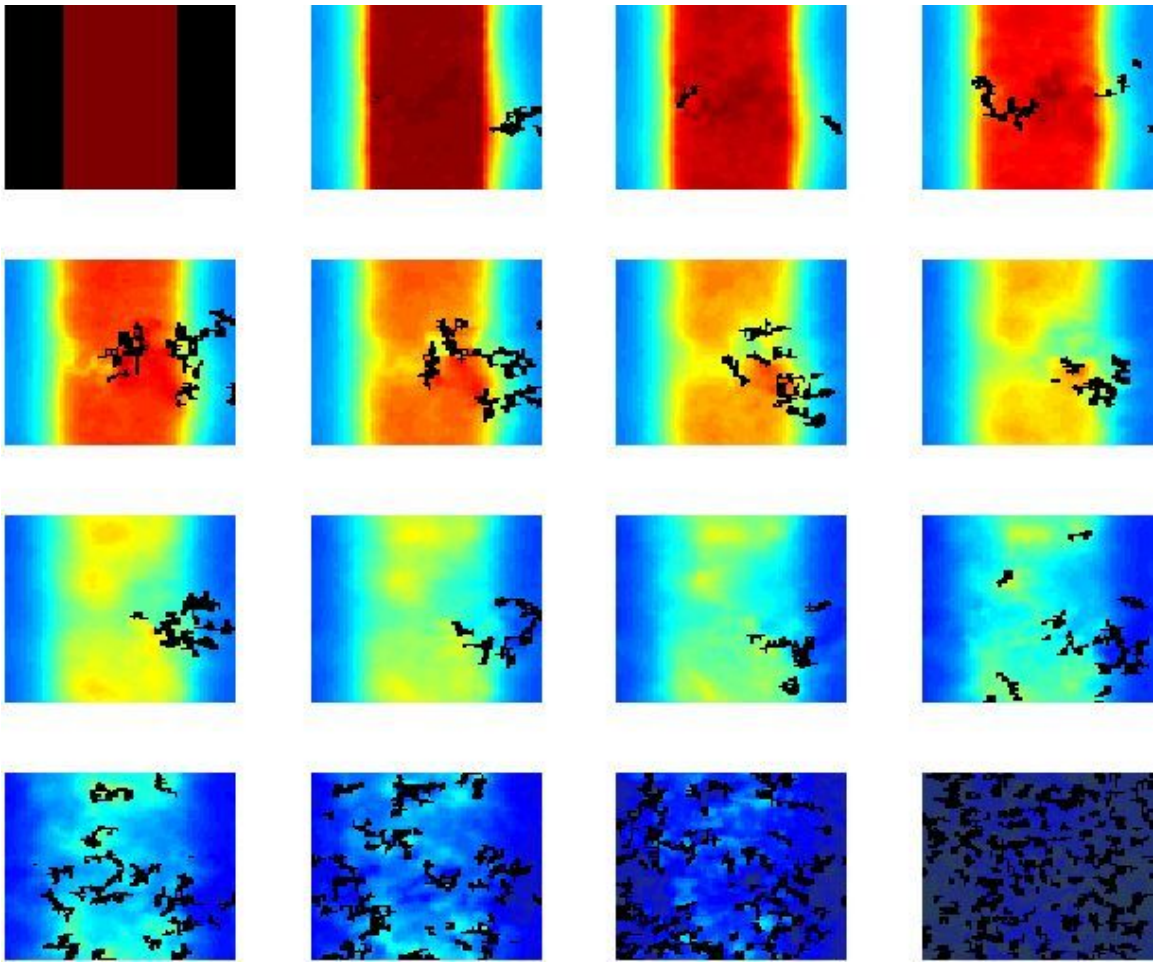

Figure 7: Liquid water and oxygen concentration distributions in various planar slices through the thickness of the GDM without an MPL for the case of water injection from the catalyst layer (bottom right panel). Color scale denotes the oxygen mole fraction in the gas phase with dark red corresponding to x_{O2} = 0.1 and dark blue denoting x_{O2} = 0. Black clusters are liquid water in the GDM pores; black bands in the top left panel are the flow field ribs.

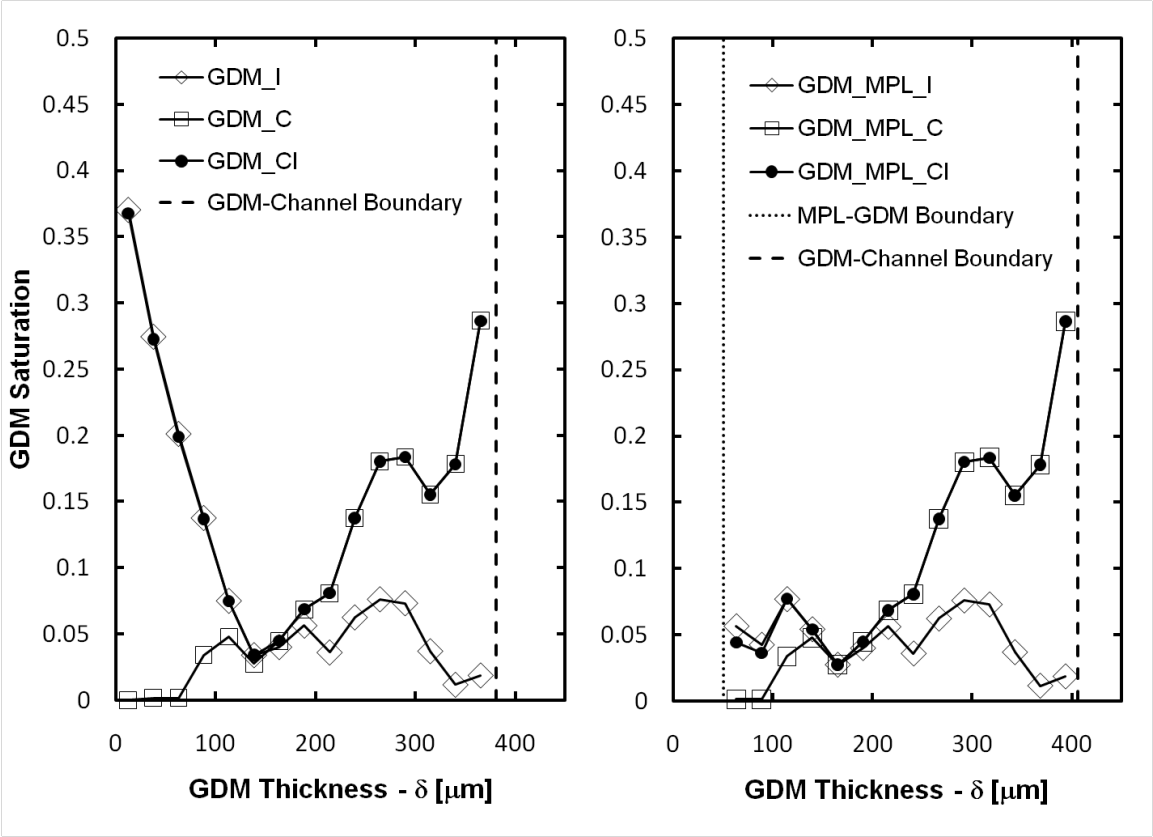

Figure 8: Liquid water saturation profiles across the GDM thickness computed for the following cases: injection (GDM_I), condensation (GDM_C) and simultaneous condensation and injection (GDM_CI) for a GDM without MPL (left) and a GDM with MPL (right).

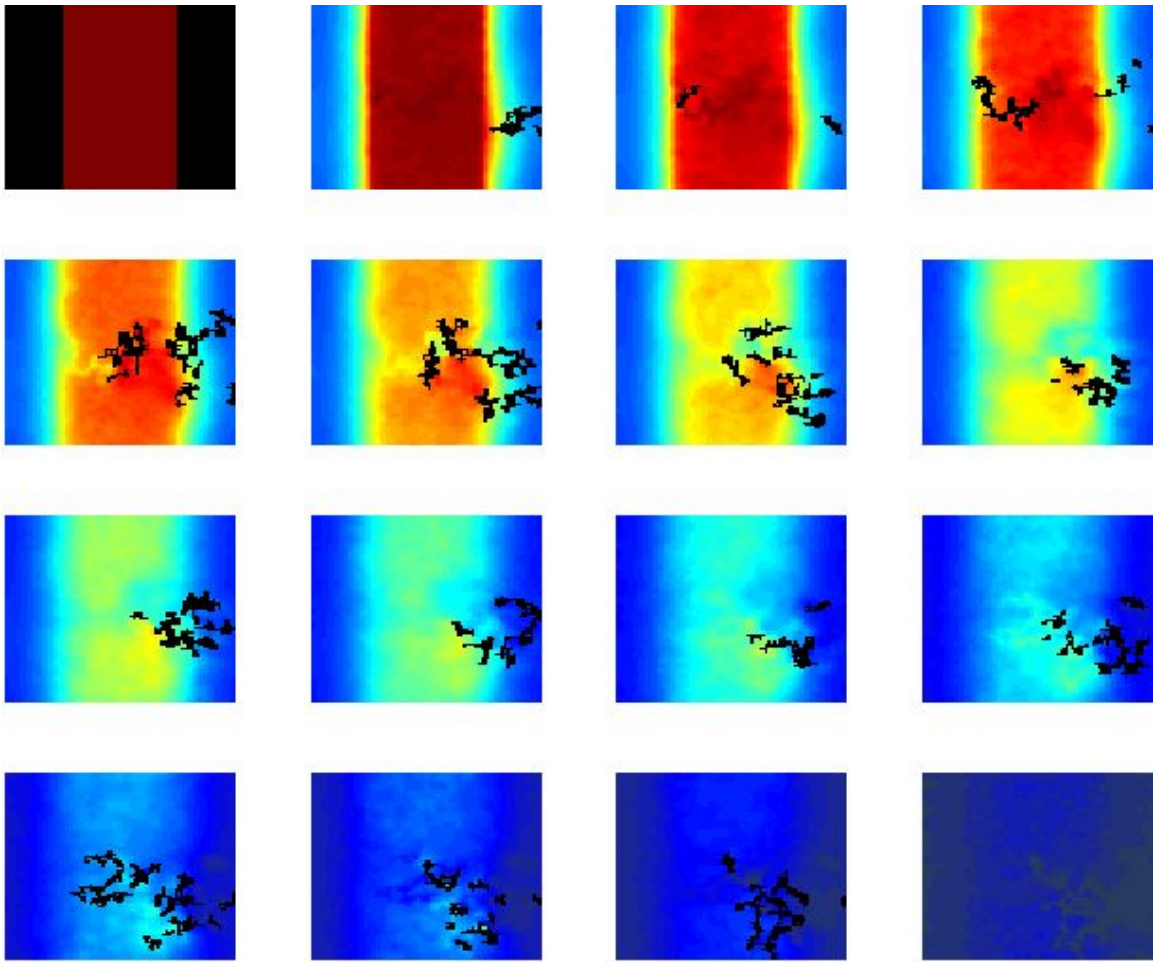

Figure 9: Liquid water and oxygen concentration distributions in various planar slices through the thickness of the GDM with an MPL for the scenario of water injection from the catalyst layer (bottom right panel). Color scale is identical to that used in Figure 7.

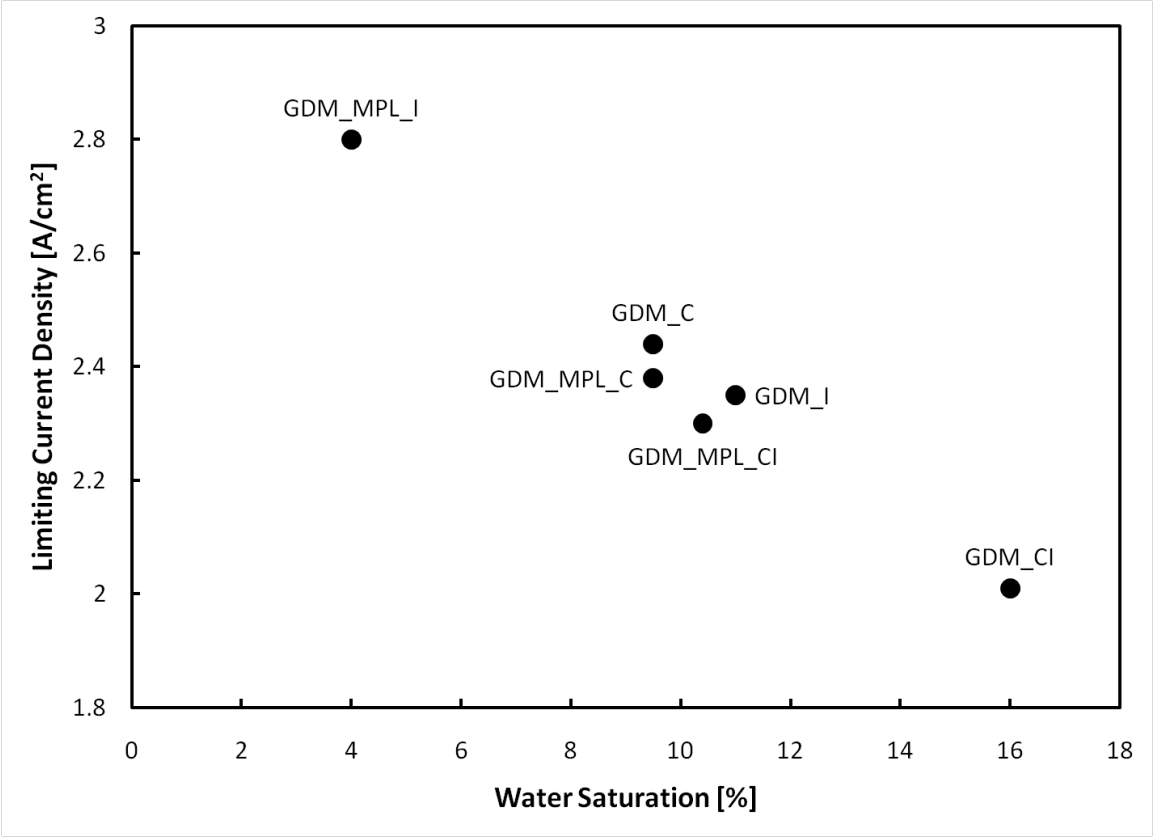

Figure 10: Relation between computed limiting current density and water saturation for various GDM combination (GDM alone and GDM with MPL) and liquid water distribution schemes (I = Injection, C = Condensation, CI = Simultaneous Condensation & Injection).

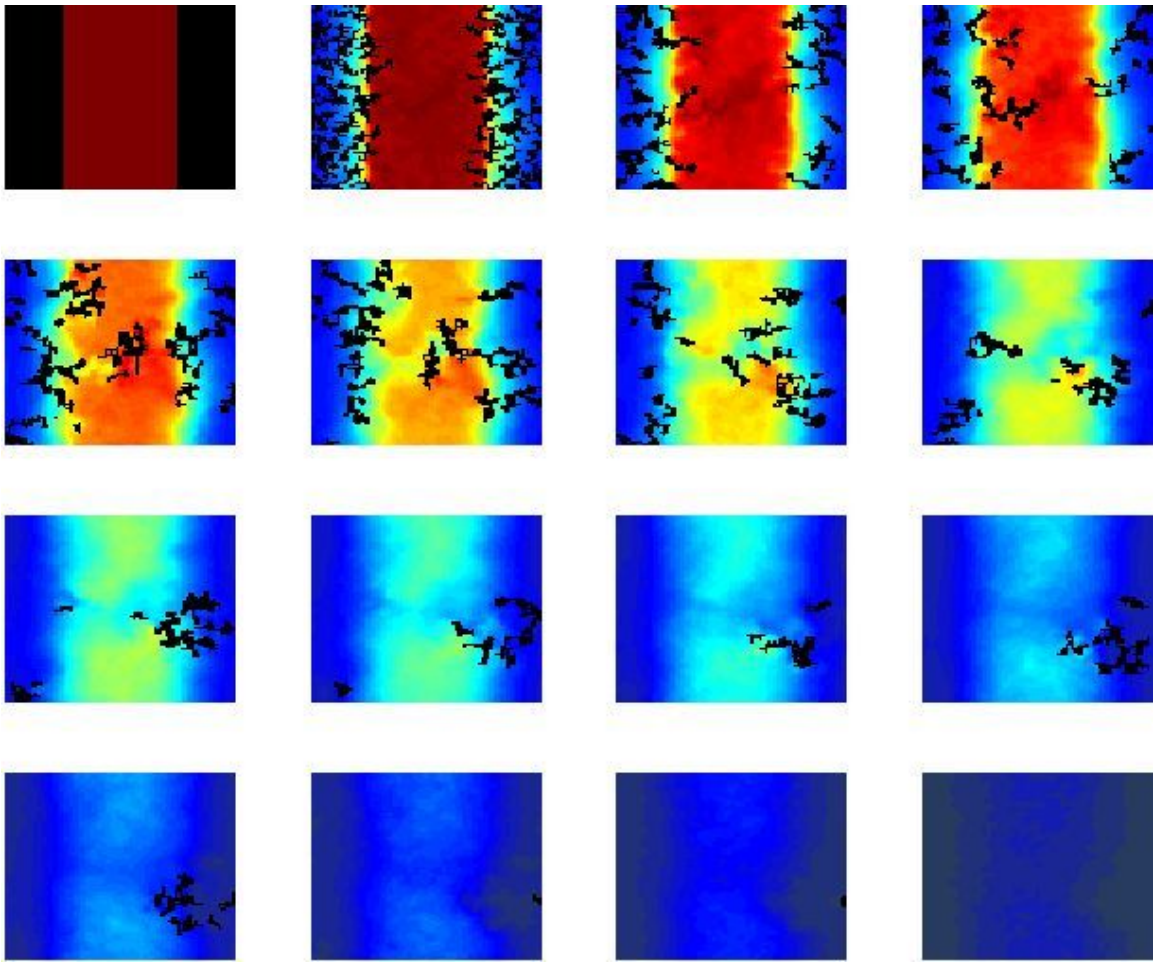

Figure 11: Liquid water and oxygen concentration distributions in various planar slices through the thickness of the GDM without an MPL for the scenario of water condensation beginning over the channel lands (top left panel). Color scale is identical to that used in Figure 7.